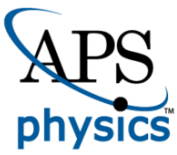

Hydraulic conductance and viscous coupling of three-phase layers in angular capillaries

H. Dehghanpour, B. Aminzadeh, and D. A. DiCarlo

Phys. Rev. E **83**, 066320 — Published 29 June 2011

DOI: 10.1103/PhysRevE.83.066320

Hydraulic conductance and viscous coupling of three-phase layers in angular capillaries

H. Dehghanpour, B. Aminzadeh, and D.A. DiCarlo*
Department of Petroleum and Geosystems Engineering, The University of Texas at Austin

Predicting three-phase relative permeability by network models requires reliable models for hydraulic conductance of films and layers stabilized by capillary forces at the pore level. We solve the creeping flow approximation of the Navier-Stokes equation for stable wetting and intermediate layers in the corner of angular capillaries by using a continuity boundary condition at the layer interface. We find significant coupling between the condensed phases and calculate the generalized mobilities by solving co-current and counter-current flow of wetting and intermediate layers. Finally, we present a simple heuristic model for the generalized mobilities as a function of the geometry and viscosity ratio.

I. INTRODUCTION

Many natural and commercial processes involve simultaneous flow of three immiscible fluids in porous media. Examples in petroleum industry include immiscible and near-miscible gas injection and water alternating gas injection (WAG) for recovery of residual oil after water flood. Furthermore, thermal methods such as cyclic steam stimulation (CSS) and steam assisted gravity drainage (SAGD) for recovery of unconventional heavy oil involves three-phase flow of mobilized oil, condensed water and vapor. Movement of nonaqueous phase liquid (NAPL) leaking from an underground storage facility toward unsaturated zone is an important example of three-phase flow in an environmental context.

The large-scale modeling of these processes require a macroscopic relationship between relative permeability and saturation. Direct measurement of three-phase relative permeability is challenging and time consuming because of the two independent saturation variables [1]. Various empirical models [2, 3] have been presented for predicting three-phase relative permeability from two-phase measurements. Predictions of these models, however, are inconsistent with experiments [4] because they do not consider the physics of three-phase flow in porous media.

During the last decade there has been much interest in predicting three-phase relative permeability by pore-scale network models [5–8]. Such models are based on capillary stability arguments, discovered displacement mechanisms and empirical models for layer conductance at the pore scale. From observations in micromodels [9–13] and capillary stability arguments based on geometry [14] and thermodynamics [15] various three-phase pore level fluid configurations and flow mechanisms have been recognized. These mechanisms have been incorporated into network models to predict three-phase relative permeability and saturation path [5, 6, 8], under the ansatz of each phase flowing independently in its own network. Depending on wettability of porous media and surface properties of the fluids, the three phases occupy different parts of the pore space. In water-wet media, water is the most wetting phase and it resides in the small pores and crevices of the pore space while gas as the most non-wetting phase occupies the center of the large pores. If the oil is spreading it forms stable intermediate layers sandwiched between gas and water. However, intermediate layers have also been observed and theoretically predicted for non-spreading oils [9, 11, 16]. Simulated relative permeability values strongly depend on hydraulic conductance of such layers.

Various methods such as hydraulic diameter [17] and thin film approximation [16] have been used to estimate the conductance of intermediate layers in the three-phase systems. Zhou et al. [18] presented a solution by combining the thin film flow and hydraulic diameter approximations. This work was extend by Firincioglu et al. [19] to account for the situations where oil and water flow simultaneously. Al-Futaisi and Patzek [20] solved the creeping flow of oil and water layers in angular capillaries numerically and presented universal curves for three-phase hydraulic conductances as a function of geometry. However, none of these works consider the coupling between phases where the potential gradient in one phase affects the flow of another phase.

Flow coupling has been investigated for two-phase flow, through experiments [21–23], analytical calculations [24–27], and simulations at the pore-scale [28, 29]. Coupled flow of wetting and non-wetting phases in angular capillaries has been solved numerically [30, 31] and semi-analytically[32] for two-phase systems.

Viscous coupling has not been studied in three-phase systems. This is surprising because flow coupling should be greater in three-phase than two-phase systems because oil in layers has a larger surface area to volume than oil in bulk.

On the macro-scale, three-phase drainage experiments [1, 33–35] show that relative permeability of oil depends on water saturation. This is commonly explained by the effect of wetting water on the pore occupancy of oil, leaving oil in larger pores with higher hydraulic conductance [1, 35]. However, in addition to the pore occupancy, the

* dicarlo@mail.utexas.edu

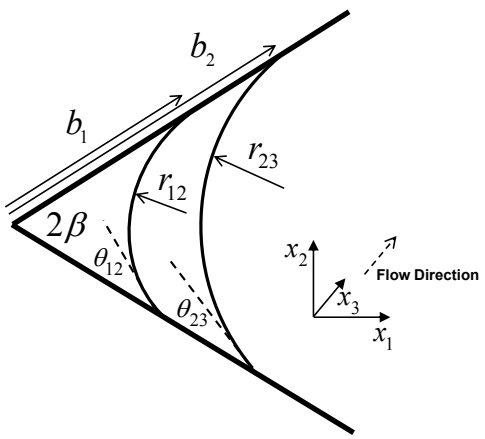

FIG. 1. Schematic illustration of water and oil layers in the corner of an angular capillary.

momentum transfer between water and oil might also play a role on the observed dependence of oil relative permeability on water saturation. In this study, we investigate this possibility.

In this manuscript, we solve the three-phase flow of wetting films and intermediate layers in the corner of angular capillaries by using finite element numerical simulation. We also obtain the generalized mobilities for various geometries and viscosity ratios. Finally, we model the mobilities as a function of the geometry and viscosity ratio from the first principles and find an appropriate match with the simulation data.

II. NON-CIRCULAR CAPILLARIES

The objective of this work is to calculate the hydraulic conductance of wetting and intermediate wetting layers stabilized by capillary forces in the corners of angular ducts. Here we assume water, oil, and gas are the wetting, intermediate, and non-wetting phases denoted by subscripts 1, 2, and 3 respectively.

A. Geometry

The geometry of two condensed phases in a corner has five degrees of freedom that is schematically depicted in Fig. 1. This geometry is defined by the corner half angle (β), the curvature and contact angle of water-oil meniscus (r_{12} and θ_{12}), and the curvature and contact angle of gas-oil meniscus (r_{23} and θ_{23}). Here, we follow the dimensionless formulations of Al-Futaisi and Patzek [20] to reduce the the number of variables and also to simplify the formulations. Furthermore, instead of using curvature radius, we use the corresponding meniscus to apex distance,

$$b_1 = r_1 \frac{cos(\theta_{12}+\beta)}{sin(\beta)}, \;\; b_2 = r_2 \frac{cos(\theta_{23}+\beta)}{sin(\beta)}. \tag{1}$$

The dimensionless meniscus to apex distances are defined by:

$$\bar{b}_1 = \frac{b_1}{b_2}, \;\; \bar{b}_2 = 1. \tag{2}$$

The dimensionless geometrical parameters of the oil and water domains such as perimeter ($\bar{p}$), area ($\bar{A}$), and meniscus length ($\bar{L}$) and layer stability criteria as a function of $(\beta, \theta_{12}, \theta_{23}, \bar{b}_1)$ are presented in the Appendix. However, not all layers that can be drawn geometrically as shown in Fig. 1 are thermodynamically stable [36]; here we consider the entire phase space of the geometrical parameters for simplicity. When used in a network model, the layers should be checked for stability.

B. Governing Equations

The equation of motion describing the two dimensional creeping flow of water, oil and gas (i.e., with negligible inertial effects) in x_3 direction with constant viscosity and density reduces to the following elliptic Poisson equation:

$$\nabla^2 v_i = -\frac{\phi_i}{\mu_i}, \;\; \forall (x_1, x_2) \in \Omega_i \quad i = 1, 2, 3 \tag{3}$$

Here v_i and μ_i are the velocity and viscosity of phase i respectively. ϕ_i is the gradient of the total driving force per unit area, which is defined by:

$$\phi_i = -\nabla P_i + \rho_i g, \tag{4}$$

where P_i is the phase pressure and g is the body force per unit mass, in this case gravity.

Following Al-Futaisi and Patzek [20], we change the variables of this equation as follows:

$$\begin{aligned} \bar{x}_i &= \frac{x_i}{b_2}, \\ \bar{\mu}_i &= \frac{\mu_i}{\mu_1}, \\ \bar{\phi}_i &= \frac{\phi_i}{\phi_1}, \\ \bar{v}_i &= \frac{v_i \, \mu_1}{\phi_1 \, b_2^2}, \quad i = 1, 2, 3. \end{aligned} \tag{5}$$

Here the dimensionless potential gradient in the water phase is unity, $\bar{\phi}_1 = 1$. The following dimensionless equations that describe the oil and water flow in the corner of the capillary are obtained by substituting the above dimensionless parameters in Eq. 3.

$$\begin{aligned} \nabla^2 \bar{v}_1 &= -1 \\ \bar{\mu}_2 \, \nabla^2 \bar{v}_2 &= -\bar{\phi}_2. \end{aligned} \tag{6}$$

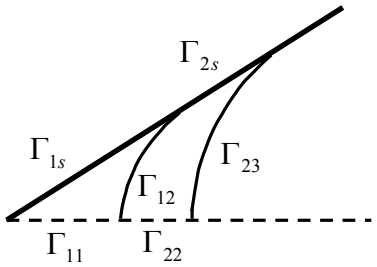

FIG. 2. Schematic illustration of the water and oil half domains and the corresponding interfaces considered for numerical modeling.

C. Boundary Conditions

The solution of Eq. 6 gives the velocity distribution across the water and oil domains (Ω_1 and Ω_2). This solution depends on the boundary conditions considered at fluid-wall interfaces (Γ_{1s} and Γ_{2s}), and fluid-fluid interfaces (Γ_{12} and Γ_{23}) that are shown in Fig. 2. The velocity at the wall is assumed to be zero according to the no-slip boundary condition, i.e.,

$$\bar{v}_i = 0 \quad on \;\; \Gamma_{is} \quad i = 1, 2. \tag{7}$$

It is enough to solve Eq. 6 for only half of the oil and water domains shown in Fig. 2. We consider null velocity gradient normal to the symmetry interface:

$$\nabla \bar{v}_i \cdot \vec{n}_i = 0 \quad on \;\; \Gamma_{ii} \quad i = 1, 2. \tag{8}$$

Here $\vec{n}_i$ is the unit vector normal to the interface.

The boundary condition at the water-oil interface is the key input for solving the velocity field. The tangential component of fluid velocity is continuous across any surface representing the interface. By considering the equations of motion for a Newtonian interface, one can relate the difference between the fluid stresses on either side of the interface to its physical properties (i.e., surface shear viscosity and surface dilational viscosity) and geometric characteristics [37].

For the two-phase systems, Ransohoff and Radke [31] and Ehrlich [32] considered the continuity of velocity and the discontinuity of shear stress at the wetting-nonwetting interface for a large range of surface shear viscosities. For the three-phase systems, Al-Futaisi and Patzek [20] considered the boundary conditions of

$$\bar{v}_i = 0 \quad on \;\; \Gamma_{12} \, or \, \Gamma_{23} \tag{9}$$

which they called the no-slip boundary condition, and the perfect-slip,

$$\nabla \bar{v}_i \cdot n_i = 0 \quad on \;\; \Gamma_{12} \, or \, \Gamma_{23} \tag{10}$$

at the oil-water and gas-oil interfaces.

The no-slip condition used by Al-Futaisi and Patzek [20] is a misnomer. It is only no-slip if one of the phases is stationary, e.g. a solid phase. Therefore, following Firincioglu et al. [19] we find it more appropriate to call Eq. 9 a no-flow boundary condition because it assumes a stationary wall between the phases that forces the velocity of each phase to be zero at the interface. The no-flow assumption can also be valid if the interfacial shear viscosity is infinite. Thus it is a reasonable boundary condition for surfactant-laden rigid water-oil interface because the molecules at the interface become bound to each other and eventually to the walls of the pore space.

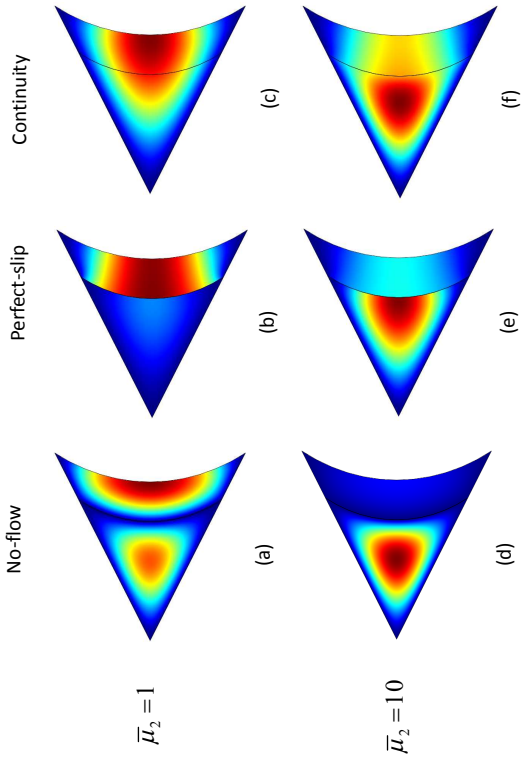

FIG. 3. The effect of the interface boundary condition on the velocity distribution of wetting and intermediate layers in an angular capillary with $\beta = \theta_{12} = \theta_{32} = 30°$, $\bar{b}_1 = 0.75$. Note that each color might represent a different velocity from one subplot to another.

The perfect-slip boundary condition which is a limiting case assumes negligible momentum transfer at the interface. This assumption is only valid if the viscosity of the neighbor phase is negligible. Thus it is a reasonable boundary condition at the gas-oil interface.

The physical boundary condition for a clean water-oil interface is the continuity of velocity and shear stress which we call the continuity boundary condition:

$$\begin{aligned} \bar{v}_1 &= \bar{v}_2 \quad on \; \Gamma_{12} \\ \nabla \bar{v}_1 \cdot n_1 &= \mu_2 \, \nabla \bar{v}_2 \cdot n_2 \quad on \; \Gamma_{12}. \end{aligned} \tag{11}$$

This boundary condition is only valid for pure fluids without any interfacial activity, which form an interface with

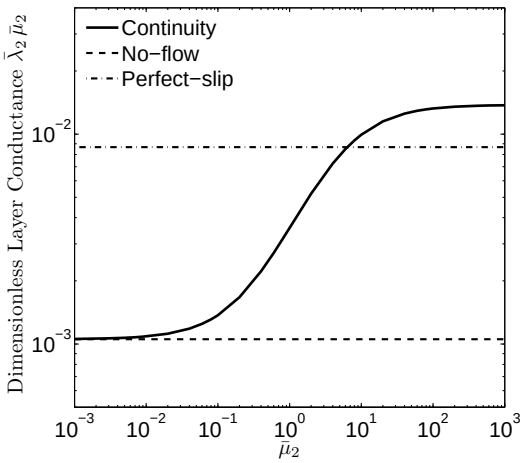

FIG. 4. The effect of the interface boundary condition on the calculated hydraulic conductance for a sandwiched oil layer in a capillary corner with $\beta = \theta_{12} = \theta_{32} = 30^\circ$ and $\bar{b}_1 = 0.75$

negligible shear viscosity [37–39].

D. Numerical Solution

We use Comsol multiphysics to solve Eq. 6 by finite element numerical simulation for the three boundary conditions of no-flow, perfect slip, and continuity at the water-oil interface. For each geometry, water and oil domains are automatically divided into triangular elements. We use the "meshrefine" application of Comsol two times to refine the initial mesh, and improve the accuracy of the numerical solution. We use the solver of "Poisson" PDE to solve the boundary value problem. For the no-flow interfaces, we use the Dirichlet boundary condition. For the perfect-slip interfaces, we use Neumann boundary condition. For the continuous interfaces, we use the "pair" application in Comsol to model the viscous coupling.

Figure 3 compares the velocity distribution across water and oil domains; in each subplot, the velocity varies between $v = 0$ (shown in dark blue) to a maximum velocity, v_{max}, (shown in dark red). However, each subplot has a different value of v_{max} and consequently a different scale. The viscosity of water and oil are identical ($\bar{\mu}_2 = 1$) in the first three subplots; the oil is ten times more viscous than water ($\bar{\mu}_2 = 10$) in the last three subplots.

In the no-flow boundary condition, (Fig. 3a and Fig. 3d), the water-oil interface behaves as a rigid wall, and the velocity of each phase increases as it moves away from the water-oil interface. Thus, the maximum velocity of the oil is at the oil-gas interface along the symmetry line, and that of water is at the center of the water film. The oil shows the same behavior in Fig. 3d, but it is more difficult to observe this behavior since in this case $\bar{\mu}_2 = 10$ and the oil velocity is 10 times less than shown in Fig. 3a.

In the perfect-slip boundary condition, (Fig. 3b and Fig. 3e), the water-oil interface behaves as perfectly lubricated, and the velocity gradient normal to the water-oil interface vanishes. Comparing Fig. 3b to Fig. 3a, we observe that the flow of oil is much greater in the perfect-slip case. This is as expected as momentum can only be transferred out through the duct wall (Γ_{2s}) which has a small length. The maximum oil velocity is again along the symmetry line, but in this case it is roughly the same at the gas-oil and oil-water interfaces. The point of maximum water velocity shifts to the right and is observed at the intersection of the water-oil interface and the symmetry line. Simply, the average flux of both phases calculated at perfect slip condition is higher than that calculated at no-flow condition because no momentum is lost at the water-oil interface.

In the continuity boundary condition, (Fig. 3c and Fig. 3f), the water-oil interface allows momentum transfer and the water and oil velocities are correlated across the interface. Because of this coupling, in Fig. 3c, water picks up velocity from oil, and in Fig. 3d oil picks up velocity from water. Therefore, for clean interfaces, the viscosity and potential gradient of the neighbor phase influence the velocity distribution of each phase.

The type of boundary condition also influences the average velocity and consequently the hydraulic conductance of the layer. We define the dimensionless total mobility by

$$\bar{q}_i = -\,\bar{\lambda}_i\,\bar{\phi}_i, \;\; i = 1, 2. \tag{12}$$

Where $\bar{q}_i$ is the dimensionless flow rate and is obtained by integrating the velocity over the flowing area:

$$\bar{q}_i = \iint\limits_{\bar{\Omega}_i} \bar{v}_i \, d\bar{A}_i, \;\; i = 1, 2 \tag{13}$$

Figure 4 compares the calculated hydraulic conductance ($\bar{\lambda}_2\,\bar{\mu}_2$) of the same oil layer shown in Fig. 3 plotted versus viscosity ratio for the three boundary conditions. According to this plot, perfect-slip and no-flow boundary conditions give conductances that are independent of viscosity ratio that means uncoupled flow of oil and water. The black solid curve, however, representing the data with the continuity boundary condition shows a strong dependence on the mid range viscosity ratio. As $\bar{\mu}_2$ decreases, the solution converges to the no-flow solution. As $\bar{\mu}_2$ increases, the solution shows a plateau that is higher than the perfect-slip limit. Therefore, for co-current flows, the no-flow boundary condition always results in the underestimation of the hydraulic conductance while the perfect-slip boundary condition depending on the viscosity ratio can lead to the overestimation or the underestimation of the hydraulic conductance.

E. Generalized Transport Coefficients

Here we assume the continuity boundary condition at the water-oil interface and the perfect-slip boundary condition at the oil-gas interface. Figures 3 and 4 indicate that the flow of each phase will drag the other phase. The total flow of each phase results from two independent driving forces. First, the potential gradient within the same phase and second, the potential gradient within the neighboring phase. The generalized Darcy equation [22, 23, 27, 40, 41] is commonly used to describe the two-phase viscous coupling in porous media. Similarly, we use the following relations to model coupled flow of the wetting and intermediate wetting phases in angular capillaries:

$$\begin{bmatrix} \bar{q}_1 \\ \bar{q}_2 \end{bmatrix} = - \begin{bmatrix} \bar{\lambda}_{11} & \bar{\lambda}_{12} \\ \bar{\lambda}_{21} & \bar{\lambda}_{22} \end{bmatrix} \begin{bmatrix} 1 \\ \bar{\phi}_2 \end{bmatrix} \tag{14}$$

Here the flow rate vector is related to the potential gradient vector by a generalized matrix of mobilities. Each mobility term represents the area open to flow, the equivalent effective permeability and also the reciprocal of the corresponding phase viscosity.

These mobilities can be calculated analytically for a simple model of circular capillary tube [33]. Here we calculate these coefficients for the creeping flow of oil and water layers in the corner of angular capillaries. Calculating the generalized mobilities for a certain geometry and viscosity ratio requires four independent equations. One possible method is to consider co-current and counter-current flow of oil and water. In the co-current case, the pressure gradients of the two phases are in the same direction while in the counter-current case, the pressure gradients are in opposite directions.

$$\begin{bmatrix} \bar{q}_1^{'} \\ \bar{q}_2^{'} \end{bmatrix} = - \begin{bmatrix} \bar{\lambda}_{11} & \bar{\lambda}_{12} \\ \bar{\lambda}_{21} & \bar{\lambda}_{22} \end{bmatrix} \begin{bmatrix} -1 \\ \bar{\phi}_2 \end{bmatrix} \tag{15}$$

The four mobility coefficients are obtained by simultaneous solution of Eq. 14 and Eq. 15. The corresponding average flow rates are obtained by integrating the calculated velocity distribution over the water and oil domains (Eq. 13) for both co-current and counter-current flows. If we assume identical potential gradients in water and oil phases ($\phi_2 = 1$), the mobilities are simply given by

$$\begin{aligned} \bar{\lambda}_{11} &= -\frac{\bar{q}_1 - \bar{q}_1^{'}}{2} \\ \bar{\lambda}_{12} &= -\frac{\bar{q}_1 + \bar{q}_1^{'}}{2} \\ \bar{\lambda}_{22} &= -\frac{\bar{q}_2 + \bar{q}_2^{'}}{2} \\ \bar{\lambda}_{21} &= -\frac{\bar{q}_2 - \bar{q}_2^{'}}{2}. \end{aligned} \tag{16}$$

The alternative approach to determine the generalized mobilities is to apply a null pressure gradient in each phase and calculate the flow rate resulting from the pressure gradient in the other phase.

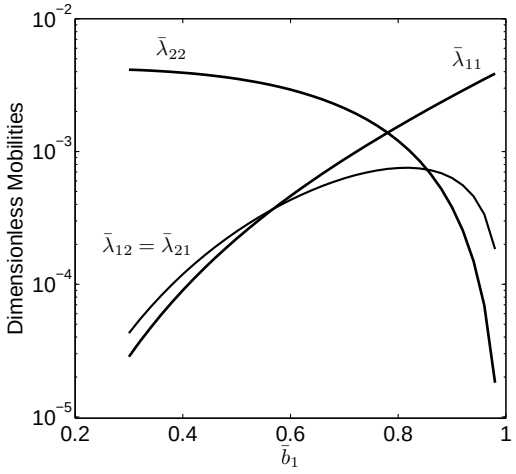

FIG. 5. Dimensionless mobilities as a function of $\bar{b}_1$ when $\beta = 30°$, $\theta_{12} = \theta_{23} = 15°$ and $\bar{\mu}_2 = 1$

The full mobilities are simply related to dimensionless values by

$$\begin{bmatrix} \lambda_{11} & \lambda_{12} \\ \lambda_{21} & \lambda_{22} \end{bmatrix} = \frac{b_2^4}{\mu_1} \begin{bmatrix} \bar{\lambda}_{11} & \bar{\lambda}_{12} \\ \bar{\lambda}_{21} & \bar{\lambda}_{22} \end{bmatrix}. \tag{17}$$

III. GENERALIZED TRANSPORT COEFFICIENTS AS A FUNCTION OF GEOMETRY AND VISCOSITY RATIO

In this section we analyze the dependence of the calculated dimensionless mobilities on the geometrical parameters and viscosity ratio. These mobilities can depend on θ_{12}, θ_{23}, β, $\bar{b}_1$, and $\bar{\mu}_2$.

Figure 5 shows the dimensionless mobilities $(\bar{\lambda}_{11}, \bar{\lambda}_{22}, \bar{\lambda}_{12})$ plotted versus $\bar{b}_1$, which indicates the relative content of water (water saturation / liquid saturation). $\bar{b}_1$ is the dominant parameter because it controls the area open to flow. We observe that the coupling terms are identical and the matrix of mobilities is symmetrical ($\bar{\lambda}_{12} = \bar{\lambda}_{21}$), which is in agreement with the Onsager reciprocal relations [42]. With increasing $\bar{b}_1$, the area open to flow of water ($\bar{A}_1$) increases and that of oil ($\bar{A}_2$) decreases and consequently the diagonal mobilities ($\bar{\lambda}_{11}$ and $\bar{\lambda}_{22}$) vary accordingly. Furthermore, with increasing $\bar{b}_1$, $\bar{\lambda}_{11}$ increases slower and $\bar{\lambda}_{22}$ decreases faster. The observed dependence of the diagonal mobilities on $\bar{b}_1$ is similar to the dependence of relative permeably on the saturation of the phase. The coupling term, $\bar{\lambda}_{12}$, however, shows a peak which corresponds to the maximum momentum transfer between the two phases. The patterns described here are similarly observed in other geometries (see Fig. 6).

Interestingly, the coupling term exceeds the diagonal

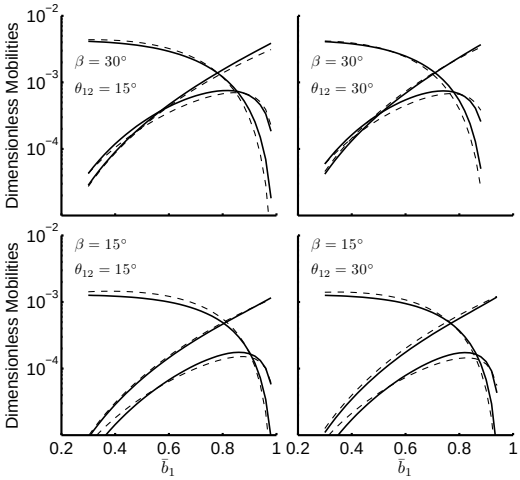

FIG. 6. Dependence of mobilities on geometry ($\theta_{23} = 15$). The solid lines show the simulated values of $\bar{\lambda}_{11}$, $\bar{\lambda}_{22}$, and $\bar{\lambda}_{12}$. The dashed lines show the predicted values by the proposed scaling models ($\bar{\mu}_2 = 1$).

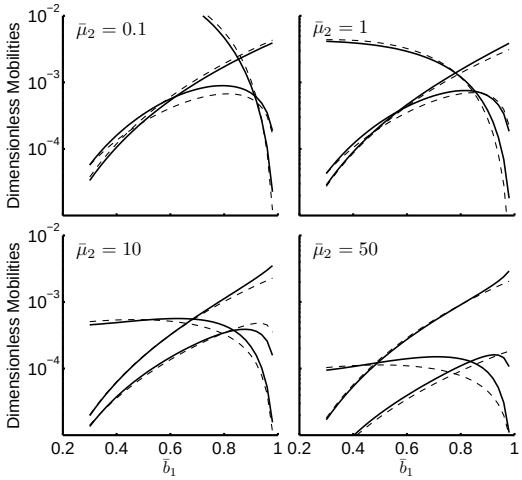

FIG. 7. Dependence of mobilities on viscosity ratio for an example geometry with $\beta = \theta_{12} = \theta_{23} = 30°$. The solid lines show the simulated values of $\bar{\lambda}_{11}$, $\bar{\lambda}_{22}$, and $\bar{\lambda}_{12}$. The dashed lines show the predicted values by the proposed scaling models.

term of oil or water at low saturations, i. e.,

$$\begin{aligned} \bar{\lambda}_{12} > \bar{\lambda}_{22} \quad when \quad 0.85 < \bar{b}_1 < 1 \\ \bar{\lambda}_{12} > \bar{\lambda}_{11} \quad when \quad 0 < \bar{b}_1 < 0.5. \end{aligned} \tag{18}$$

When the thickness of the oil or water layers decreases, viscous coupling dominates the flow and thus the fluid with high saturation drags the fluid with low saturation.

Figure 6 shows how the mobilities vary when β and θ_{12} change. Each subplot shows the mobilities as a function of $\bar{b}_1$. Between the plots, we alter β and θ_{12}. We increase β from 15° in the bottom subplots to 30° in the top subplots, and θ_{12} from 15° in the left subplots to 30° in the right subplots.

When other parameters are constant, the three mobilities increase by increasing β from 15° to 30°. This is an expected behavior as the area open to flow of both water and oil increases by increasing β. When β increases, the $\bar{b}_1$ value where $\bar{\lambda}_{12}$ exceeds $\bar{\lambda}_{22}$ decreases. Furthermore, the top subplots ($\beta = 30$) show that $\bar{\lambda}_{12} > \bar{\lambda}_{11}$ when $\bar{b}_1 < 0.5$ while in the bottom subplots ($\beta = 15$), $\bar{\lambda}_{12}$ does not exceed $\bar{\lambda}_{11}$. At higher values of β, the water-oil interface is larger and thus viscous coupling becomes more important.

The contact angle also affects the area open to flow but its effect is smaller than that of β and $\bar{b}_1$. For example, increasing θ_{12} from 15° to 30° only slightly increases $\bar{\lambda}_{11}$ and decreases $\bar{\lambda}_{22}$. We also observe that when θ_{12} increases, the $\bar{b}_1$ value where $\bar{\lambda}_{12}$ exceeds $\bar{\lambda}_{22}$ decreases slightly.

Figure 7 shows the dependence of mobilities on the viscosity ratio for the same geometry as Fig. 5. When $\bar{\mu}_2 = 0.1$ and $\bar{b}_1 < 0.6$, water is mainly flowing by the oil gradient, i.e., $\bar{\lambda}_{12} > \bar{\lambda}_{11}$. When $\bar{\mu}_2 = 10$ and $\bar{b}_1 > 0.85$ oil is mainly flowing by the water gradient, i.e., $\bar{\lambda}_{12} > \bar{\lambda}_{22}$. Furthermore, When $\bar{\mu}_2$ increases from 0.1 to 10, the $\bar{b}_1$ value where $\bar{\lambda}_{12}$ exceeds $\bar{\lambda}_2$ reduces from 0.95 to 0.85. We conclude that the contribution of coupling on the flow of each phase increases when the relative viscosity of the phase increases. Therefore, a comprehensive model for the generalized mobilities would have both the geometry and viscosity ratio.

IV. SCALING MODELS FOR GENERALIZED MOBILITIES

The objective of this section is to model the generalized mobilities as a function of the geometry and viscosity ratio, $(\beta, \theta_{12}, \theta_{23}, \bar{b}_1, \bar{\mu}_2)$. Al-Futaisi and Patzek [20] proposed universal curves for the intermediate layer conductance, as a function of the geometrical parameters only, by running extensive numerical simulations and using projection-pursuit regression. We extend this work to account for the flow coupling between oil and water. Furthermore, instead of statistical regression models, we present a simple heuristic model based on the scaling arguments from fluid mechanics.

A. Diagonal Terms

We use the concept of hydraulic radius, which is used to describes the dependence of laminar flow rate on pressure gradient in non-circular ducts:

$$q = \frac{c}{\mu} A R_h^2 \phi. \tag{19}$$

Hydraulic radius, R_h, is defined as the area open to flow, A, divided by wetted perimeter, p_w.

$$R_h = \frac{A}{p_w} \tag{20}$$

The constant c depends on the shape of the ducts. For a circular tube $c = \frac{1}{2}$ (Poiseuille's law) and for flow between parallel plates $c = \frac{2}{3}$ (cubic law).

The dimensionless form of Eq.19 is given by

$$\bar{q} = \frac{c}{\bar{\mu}} \bar{A} \, (\frac{\bar{A}}{\bar{p}_w})^2 \, \bar{\phi}. \tag{21}$$

By analogy with this equation we propose the following expressions for diagonal mobilities:

$$\begin{aligned} \bar{\lambda}_{11} &= c_{11} \, \frac{(\bar{A}_1)^3}{(\bar{p}_{1w})^2} \\ \bar{\lambda}_{22} &= \frac{c_{22}}{\bar{\mu}_2} \, \frac{(\bar{A}_2)^3}{(\bar{p}_{2w})^2} \end{aligned} \tag{22}$$

The wetted perimeter is the length of the fluid-wall interface where the velocity is zero and stress is non-zero. For example, in an open duct, the fluid-air interface where the drag is zero is not considered as part of the wetted perimeter. In the corner geometry, the fluid-wall interface (Γ_{1s} and Γ_{2s}) is considered as part of the wetted perimeter, but the oil-water interface (Γ_{12}) could be considered wetted, non-wetted or something in between, thus should depend on the viscosity ratio. If $\bar{\mu}_2 \gg 1$, the water is inviscid compared to the oil and the wetted perimeter for oil domain ($\bar{p}_{2w}$) does not include Γ_{12} likewise that of water domain ($\bar{p}_{1w}$) includes the Γ_{12}. Similarly, if $\bar{\mu}_2 \ll 1$, $\bar{p}_{2w}$ includes Γ_{12}, and $\bar{p}_{1w}$ does not include the Γ_{12}. Therefore, for the mid range viscosity ratio, the wetted perimeter should be a function of $\bar{\mu}_2$:

$$\begin{aligned} \bar{p}_{2w} &= 2(1 - \bar{b}_1) + \bar{L}_{12} \times f(\bar{\mu}_2) \\ \bar{p}_{1w} &= 2\bar{b}_1 + \bar{L}_{12} \times f(\frac{1}{\bar{\mu}_2}). \end{aligned} \tag{23}$$

We consider the following limits for $f(x)$.

$$\begin{aligned} f(x) = 0 \quad when \;\; x \longrightarrow \infty \\ f(x) = 1 \quad when \;\; x \longrightarrow 0 \end{aligned} \tag{24}$$

Various decay functions such as e^{-x} and $1/(1+x^n)$ meet the above boundary condition. Using the values of area and interface length in the Apendix, we find that $f(x) = e^{-\sqrt{x}}$ fits the data. Our simulation results show that the best values for c_{11} and c_{22} are $\frac{4}{5}$ and $\frac{1}{2}$, respectively.

B. Coupling Term

We use the concept of momentum balance to develop an expression that relates the flow of water, q_1, to the potential gradient in the oil phase, ϕ_2, when $\phi_1 = 0$. Here, the only driving force for the water flow is the shear stress transferred to the water, τ_{12}, at the interface. Therefore, an expression is required for flow through a duct under an external shear stress. The simplest case is the two-dimensional creeping flow between two parallel plates under the fixed shear stress, τ_s, applied to one of the plates. By solving the Stokes equation for this problem, we have:

$$q = \frac{w\,\delta}{\mu} \, \frac{\delta}{2} \, \tau_s \tag{25}$$

Here w, is the plate width and δ is the spacing between the two plates. The resulting flow rate, q, is related to the applied shear stress by the area open to flow, $w\,\delta$ and the wetted perimeter, $\frac{\delta}{2}$. Equivalently, the flow of water due to the momentum transfer across the water-oil interface is approximated by:

$$q_1 = \frac{c_{12}}{\mu_1} \, A_1 \, \frac{A_1}{p_{1w}} \, \tau_{12} \tag{26}$$

Here we define a similarity coefficient (c_{12}) which depends on the geometry of the corner and layer. With decreasing corner half angle β, $\bar{\lambda}_{12}$ sharply decreases (see Fig. 6). The length of the water-oil interface increases as β increases, which results in higher momentum transfer between the two phases. Our simulation results show that the best value for c_{12} is β in radians.

An expression is also needed to relate τ_{12} to the geometry, viscosity ratio and potential gradient within the oil phase. The amount of momentum transferred at the oil-water interface is a fraction of the total momentum that is driving the oil phase. This fraction depends on the geometry and viscosity ratio, $g(\bar{\mu}_2)$. First, we approximate the stress transferred to the interface at extreme values of $\bar{\mu}$. We assume that the momentum transferred to the water is negligible, $\tau_{12} \approx 0$, when $\bar{\mu}_2 \gg 1$. On the other hand, when $\bar{\mu}_2 \ll 1$, we assume that the potential gradient in the oil phase is uniformly transferred to the the perimeter, i. e., $\tau_{12} = \frac{\phi_2 \, A_2}{p_2}$. Therefore, τ_{12} and ϕ_2 can be related by:

$$\tau_{12} = g(\bar{\mu}_2) \, \frac{A_2}{p_{2w}} \, \phi_2. \tag{27}$$

By substituting Eq. 26 in Eq. 27 we arrive at the following dimensional equation that gives the flow of water due to the pressure gradient in the oil phase:

$$q_1 = \beta \, \frac{g(\bar{\mu}_2)}{\mu_1} \, A_1 \, \frac{A_1}{p_{1w}} \, \frac{A_2}{p_{2w}} \, \phi_2 \tag{28}$$

Finally, the dimensionless coupling term is given by:

$$\bar{\lambda}_{12} = \frac{\bar{q}_1}{\bar{\phi}_2} = \frac{\beta}{\bar{p}_{1w} \, \bar{p}_{2w}} \bar{A}_1^2 \, \bar{A}_2 \, g(\bar{\mu}_2). \tag{29}$$

We examine the dependence of $\bar{\lambda}_{12}$ on $\bar{\mu}_2$ in Fig. 8 to find a good $g(\bar{\mu}_2)$. We know that at extreme values of $\bar{\mu}_2$, $\bar{p}_{1w}$ and $\bar{p}_{2w}$ are independent of $\bar{\mu}_2$. Therefore, $\bar{\lambda}_{12}$

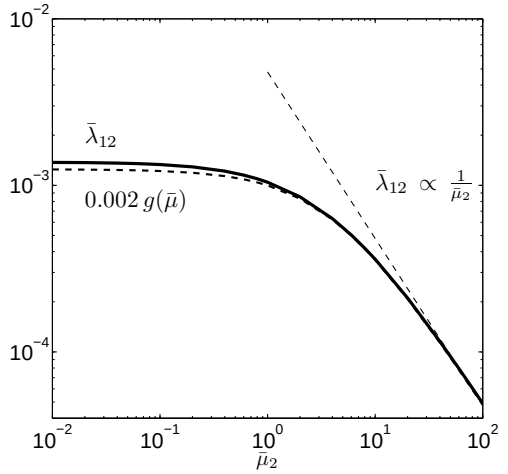

FIG. 8. The dependence of $\bar{\lambda}_{12}$ on $\bar{\mu}_2$ for an example geometry with $\beta = \theta_{12} = \theta_{23} = 30^\circ$ and $\bar{b}_1 = 0.75$. $g(u) = \frac{2.5}{4+\bar{\mu}_2}$ matches the dependence of $\bar{\lambda}_{12}$ on $\bar{\mu}_2$.

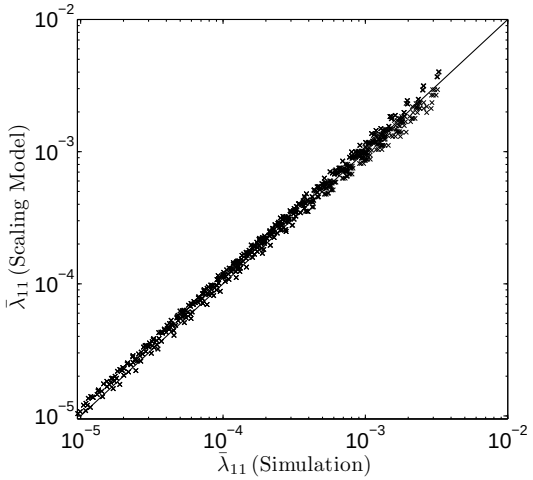

FIG. 9. Predictions of the scaling model versus simulated values of $\bar{\lambda}_{11}$

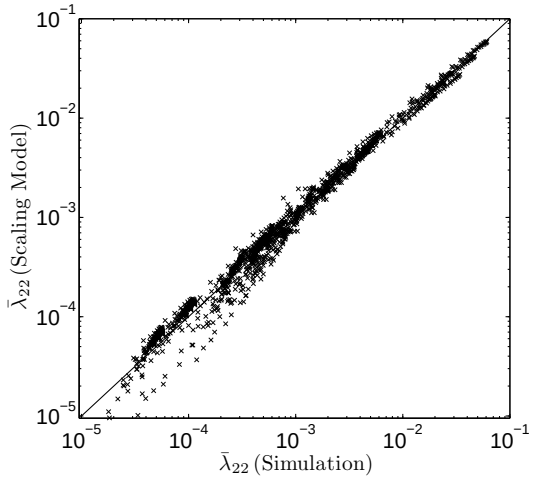

FIG. 10. Predictions of the scaling model versus simulated values of $\bar{\lambda}_{22}$

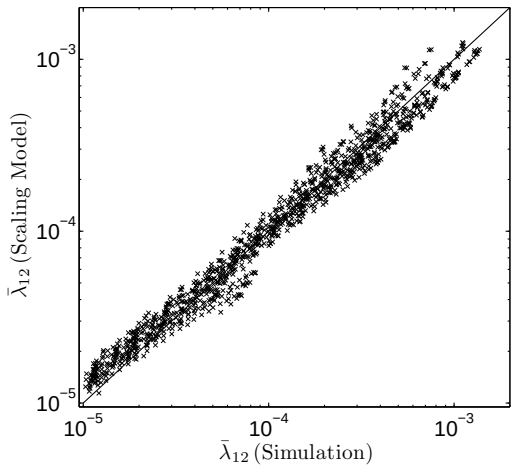

FIG. 11. Predictions of the scaling model versus simulated values of $\bar{\lambda}_{12}$

and $g(\bar{\mu}_2)$ should similarly depend on $\bar{\mu}_2$ at the limits. According to Fig. 8, at high values of $\bar{\mu}_2$ ($\bar{\mu}_2 > 10$), $\bar{\lambda}_{12} \propto \frac{1}{\bar{\mu}_2}$. At low values of $\bar{\mu}_2$ ($\bar{\mu}_2 < 0.1$), $\bar{\lambda}_{12}$ is independent of $\bar{\mu}$. Fig. 8 shows that $\frac{1}{4+\bar{\mu}_2}$ matches the dependence on $\bar{\mu}_2$. We find that using $g(\bar{\mu}_2) = \frac{2.5}{4+\bar{\mu}_2}$ gives a good fit to the data for all geometries.

C. Model Validation

The predictions of the suggested models are shown by dashed lines in Figs. 6 and 7. Figure 6 shows that the presented models appropriately match the functional dependence of $\bar{\lambda}_{11}$, $\bar{\lambda}_{22}$ and $\bar{\lambda}_{12}$ on $\bar{b}_1$ for the four different example geometries when $\bar{\mu}_2 = 1$. Fig 7 shows that these models work very well when $\bar{\mu}_2$ varies from 0.1 to 50. We also created 1376 simulated mobilities by changing β, θ_{12} and θ_{23} from 10° to 30°, $\bar{b}_1$ from 0.3 to 0.95 and $\bar{\mu}_2$ from 0.1 to 10, to test the performance of the presented models. Figures 9, 10 and 11 show that the predicted values of $\bar{\lambda}_{11}$, $\bar{\lambda}_{22}$ and $\bar{\lambda}_{12}$ are fairly close to the simulated values. We calculated the relative error ($E_{\bar{\lambda}_{ij}}$) for each mobility by:

$$E_{\bar{\lambda}_{ij}} = \frac{|\bar{\lambda}_{ij}^{sim} - \bar{\lambda}_{ij}^{model}|}{\bar{\lambda}_{ij}^{sim}}, \;\; i, j = 1, 2. \qquad (30)$$

Here $\bar{\lambda}_{ij}^{sim}$ is the simulated value, and $\bar{\lambda}_{ij}^{model}$ is calculated by the proposed scaling model. The mean values of relative error for $\bar{\lambda}_{22}$, $\bar{\lambda}_{11}$, and $\bar{\lambda}_{12}$ are found to be 16%, 11%, 24% respectively.

V. DISCUSSION

By incorporating the continuity boundary condition at the oil-water interface, we have calculated the flow of water and oil in the layers that form in pore corners. The major results can be summarized as follows

1. The flow of oil and water are viscously coupled in three-phase flow.

2. For a particular phase, the amount of flow caused by viscous coupling can be greater than that caused by a pressure gradient within the phase.

3. The dependence of the conductivity on the geometry of the corner, the size of the layers, and the viscosity ratio can be modeled successfully using simple scaling arguments.

In particular, results 1 and 2 show that the coupling contribution to the overall flow can be relatively large for three-phase flow. This is due to the fact that the ratio of oil/water interface to oil volume is much greater in three-phase flow than in two-phase flow. Essentially gas can occupy the center of the pore, decreasing the oil volume for the same amount of oil/water interface. Thus the momentum dissipation in an oil layer is primarily through the water phase, which in turn can flow. Onsager reciprocity ensures that the coupling works both ways; i.e. from the water to the oil phase. In contrast, for two-phase flow there is flow coupling, but to a much smaller extent. This is because for the two-phase geometry, layers do not form for uniform wettability conditions, and the ratio of oil/water interface to oil volume is relatively small. The momentum is primarily dissipated into the immobile solid in this case. However, in certain pore geometries such as star-shape pores [43] oil/water interface can be much larger than oil/solid interface even for a two phase system. Furthermore, oil layers, sandwiched between water in corners and in the center of a capillary with non-uniform wettability, can be thermodynamically stable [15]. In these cases, viscous coupling may be significant for two-phase systems at certain conditions. This remains to be studied.

Result 3 is important for modeling multi-phase flow in porous media. Currently, this is often done using network modeling [5, 6, 8]. These network models involve obtaining a network (from images or grain settling simulation), and for multi-phase flow, obtaining an occupancy of each phase in each element of the model. The total permeability of each phase is calculated from the conductivities of each phase in the elements of the network. Result 3 gives a straightforward method to calculate the liquid conductivities in the layers that exist in gas filled elements using the continuity boundary condition. These fluid layers are thermodynamically stable [15], and has been implicated as a major source of oil relative permeability at low oil saturations in three-phase flow [16, 44]. Using these results and a three-phase network model, the effects of flow coupling on macroscopic relative permeabilities should now be able to be estimated.

The existing experimental data on three-phase relative permeability [1, 34, 35] shows that oil relative permeability in water-wet systems depends on oil and water saturations, which is traditionally explained by the pore scale distribution of wetting and intermediate phases. However, the viscous coupling between the wetting and intermediate phases can also result in the dependence of oil relative permeability on water saturation. It will be interesting to see whether network models can reproduce the observed experimental behavior by incorporating the layer viscous coupling.

As mentioned in the model development, while the continuity condition at the oil-water interface is physically correct for pure fluids with no surface activity there remains the question of the correct boundary condition at the interface. Clearly, momentum and velocity should be continuous across the interface (the continuity condition). But for fluids with natural or artificial surfactants, there can be an additional interfacial shear viscosity that can be relevant. For pure fluids, there are little or no interfacial agents, and thus the continuity condition solved for in this manuscript is also appropriate. Since all three-phase experiments [1, 19, 44, 45] have been conducted using pure fluids, they should be modeled using the correct continuity boundary condition. These experiments all have either co-current or counter-current liquid phases.

Crude oils, which are mixtures, have the potential to have naturally occurring surfactants. The additional interfacial shear viscosity has been measured for several crude oils [46]. Analytical analysis of Wasan et al. [38] shows that increasing interfacial shear viscosity at either the liquid-liquid or the liquid-gas interface results in lower velocity at the liquid-liquid interface in three-phase systems. This can have the effect of making the interface more of a no-flow ($v = 0$) boundary rather than a continuity boundary. A non-zero interfacial shear viscosity will cause an effective discontinuity in the momentum transfer across curved interfaces like those seen in angular corners. Essentially a portion of the momentum across the interface will be transferred to the solid walls through the interfacial shear viscosity. On the other hand, addition of artificial surfactants to a water-oil system can reduce the interfacial viscosity. These effects have been studied in two-phase flow by Gupta and Wasan [47] who showed that by applying some surfactants in a mixed surfactant system, the interfacial shear viscosity can be reduced. For core floods, this enhances the permeability of the oil phase through flow coupling [48]. The work in the current manuscript suggests that this phenomena would be much greater for three-phase flow due to the flow coupling being much greater in three-phase than two-phase flow. The effect of interfacial shear viscosity in three-phase layers can be studied using the same techniques outlined in this manuscript.

In summary, we have numerically simulated flow in capillary-stabilized water and oil layers in angular cor-

ners by using the physically correct continuity boundary condition at the water-oil interface. We find significant flow coupling and present a simple scaling model that can be used to estimate the layer conductivities.

ACKNOWLEDGMENTS

We thank N. Hajari, R. Johns and L. Lake for discussions. H.D. acknowledge support from the Industrial Associates Gas Flooding Program at The University of Texas at Austin. B.A. and D.D. acknowledge support from the Center for Frontiers of Subsurface Energy Security, an Energy Frontier Research Center funded by the U.S. Department of Energy, Office of Basic Energy Sciences under Award Number DE-SC0001114.

VI. APPENDIXES

Al-Futaisi and Patzek [20] used the following parameters to simplify the expressions for dimensionless area, perimeter and arc length:

$$\begin{aligned} E_0^{ij} &= \frac{\pi}{2} - \theta_{ij} - \beta \\ E_1^{ij} &= \frac{\cos(\theta_{ij}+\beta)}{\sin\beta} \\ E_2^{ij} &= \frac{\cos(\theta_{ij}+\beta)}{\sin\beta}\cos\theta_{ij} \\ i &= 1,2,3,\ j \neq i \end{aligned} \tag{31}$$

If $\theta_{12}+\beta = \pi/2$, the dimensionless cross-sectional area of wetting ($\bar{A}_1$) and intermediate wetting phase ($\bar{A}_2$)and the length of water-oil interface ($\bar{L}_{12}$) is given by:

$$\begin{aligned} \bar{A}_1 &= \bar{b}_1^2 \sin\beta\,\cos\beta \\ \bar{A}_2 &= \frac{E_2^{32} - E_0^{32}}{(E_1^{32})^2} - \bar{A}_1 \\ \bar{L}_{12} &= 2\,\bar{b}_1 \sin\beta, \end{aligned} \tag{32}$$

Otherwise,

$$\begin{aligned} \bar{A}_1 &= \bar{b}_1^2 \frac{E_2^{21} - E_0^{21}}{(E_1^{21})^2} \\ \bar{A}_2 &= \frac{E_2^{32} - E_0^{32}}{(E_1^{32})^2} - \bar{A}_1 \\ \bar{L}_{12} &= 2\,\bar{b}_1\,\frac{E_0^{21}}{E_1^{21}}. \end{aligned} \tag{33}$$

The dimensionless length of gas-oil interface ($\bar{L}_{23}$) is given by:

$$L_{23} = 2\,\frac{E_0^{32}}{E_1^{32}}. \tag{34}$$

The dimensionless perimeter of water and oil domain are given by:

$$\begin{aligned} \bar{p}_1 &= 2\,\bar{b}_1 + \bar{L}_{21} \\ \bar{p}_2 &= 2\,(1-\bar{b}_1) + \bar{L}_{12} + \bar{L}_{23} \end{aligned} \tag{35}$$

$\bar{b}_1$ must be higher than a threshold value to have a stable layer in the corner. If $\theta_{12}+\beta = \pi/2$,

$$\bar{b}_1 \geq \frac{1}{\cos^2\beta}[1 - \frac{\cos\beta}{E_1^{32}} + \frac{\cos\beta\sin\theta_{32}}{E_1^{32}}], \tag{36}$$

otherwise,

$$\bar{b}_1 \geq \min\{1, |\frac{E_1^{21}}{E_1^{32}}\frac{\cos\theta_{32} - \sin\beta}{\cos\theta_{21} - \sin\beta}|\}. \tag{37}$$

[1] M. J. Oak, L. E. Baker, and D. C. Thomas, J. Pet. Technol. **42**, 1054 (1990).
[2] H. L. Stone, J. Can. Pet. Technol. **12**, 53 (1973).
[3] H. L. Stone, J. Pet. Technol. **22**, 241 (1970).
[4] L. Oliveira and A. H. Demond, J. Contam. Hydrol. **66**, 261 (2003).
[5] M. Piri and M. J. Blunt, Phys. Rev. E **71**, 026301 (2005).
[6] M. I. J. van Dijke and K. S. Sorbie, Phys. Rev. E **66**, 046302 (2002).
[7] V. Mani and K. K. Mohanty, SPEJ , 238 (1998).
[8] D. H. Fenwick and M. J. Blunt, Adv. Water Resour. **21**, 121 (1998).
[9] P. V. R. A. A. Keller, M. J. Blunt, Transp. in Porous Media **20**, 105 (1997).
[10] W. E. Soll, M. A. Celia, and J. L. Wilson, Water Resour. Res. **29**, 2963 (1993).
[11] M. Dong, F. A. Dullien, and I. Chatzis, J. Colloid Interf. Sci. **172**, 278 (1995).
[12] P. E. Oren and W. V. Pinczewski, Transp. in Porous Media **20**, 105 (1995).
[13] P. E. Oren, J. Billiotte, and W. V. Pinczewski, SPE Form. Eval. **7**, 70 (1992).
[14] M. H. Hui and M. J. Blunt, J. Phys. Chem. **104**, 3833 (2000).
[15] M. I. J. van Dijke and K. S. Sorbie, J. Colloid Interf. Sci. **293**, 455 (2006).
[16] M. J. Blunt, D. Zhou, and D. H. Fenwick, Transp. Porous Media **20**, 77 (1995).
[17] R. Lenormand and C. Zarcone, in *59th Annual Meeting of the SPE* (Houston, TX, USA, 1984).
[18] D. Zhou, M. J. Blunt, and F. M. Orr, J. Colloid Interf. Sci. **187**, 11 (1997).

[19] T. Firincioglu, M. J. Blunt, and D. Zhou, Colloids surf. A **155**, 259 (1999).

[20] A. Al-Futaisi and T. W. Patzek, SPEJ **8**, 252 (2003).

[21] F. A. L. Dullien and M. Dong, Transp. in Porous Media **25**, 97 (1996).

[22] R. G. Bentsen and A. A. Manai, Transp. in Porous Media **11**, 243 (1993).

[23] D. G. Avraam and A. C. Payatakes, Transp. in Porous Media **20**, 135 (1995).

[24] S. M. Hassanizadeh and W. Gray, Adv. Water Resour. **3**, 25 (1980).

[25] S. M. Hassanizadeh and W. Gray, Adv. Water Resour. **2**, 131 (1979).

[26] S. Whitaker, Transp. in Porous Media **1**, 105 (1986).

[27] F. Kalaydjian, Transp. in Porous Media **2**, 537 (1987).

[28] H. Huang and X. Y. Lu, Phys. Fluids **21** (2009).

[29] H. Li, C. Pan, and C. T. Miller, Phys. Rev. E **72**, 026705 (2005).

[30] T. W. Patzek and J. G. Kristensen, J. Colloid Interf. Sci. **236**, 305 (2001).

[31] T. C. Ransohoff and C. J. Radke, J. Colloid Interf. Sci. **121** (1988).

[32] R. Ehrlich, Transp. in Porous Media **11**, 201 (1993).

[33] H. Dehghanpour, B. Aminzadeh, and D. A. DiCarlo, Phys. Rev. E In press.

[34] E. C. Donaldson and G. W. Dean, U. S. Bureau of Mines (1966).

[35] M. Honarpour, L. Koederitz, and A. H. Harvey, *Relative Permeability of Petroleum Reservoirs*, 3rd ed. (CRC, 1986).

[36] M. I. J. van Dijke, M. Lago, K. S. Sorbie, and M. Araujo, J. Coll. Interf. Sci. **277**, 184 (2004).

[37] L. E. Scriven, Chem. Eng. Sci. **12**, 98 (1960).

[38] D. T. Wasan, L. Gupta, and M. K. Vora, AIChE J. **17**, 1287 (1971).

[39] D. J. Stoodt and J. C. Slattery, AIChE J. **30**, 564 (1984).

[40] J. L. Auriault and E. Sanchez-Palencia, J. Theor. Appl. Mech. special issue , 141 (1986).

[41] W. Rose, Transp. in Porous Media **3**, 163 (1988).

[42] L. Onsager, Phys. Rev. **37**, 405 (1931).

[43] O. Frette and J. Helland, Adv. Water Resour. **33**, 846 (2010).

[44] D. A. DiCarlo, A. Sahni, and M. J. Blunt, Transp. in Porous Media **39**, 347 (2000).

[45] A. Sahni, J. E. Burger, and M. J. Blunt (SPE/DOE Improved Oil Recovery Symposium, Tulsa, OK, USA, 1998).

[46] D. T. Wasan and V. Mohan, in D. O. Shah and R. S. Schechter, (eds), Improved oil recovery by surfactant and polymer flooding, Academic Press, New York , 161 (1977).

[47] L. Gupta and D. T. Wasan, Ind. Eng. Chem. fundam. **13**, 26 (1974).

[48] E. A. Knaggs (ACS Marketing Symp., New York, N. Y., 1976).